Letter

Moiré induced topology and flat bands in twisted bilayer WSe_2: A first-principles study

Sudipta Kundu, Mit H. Naik,* H. R. Krishnamurthy, and Manish Jain
Center for Condensed Matter Theory, Department of Physics, Indian Institute of Science, Bangalore 560012, India

(Received 30 April 2021; accepted 24 January 2022; published 17 February 2022)

We study the influence of strong spin-orbit interaction on the formation of flat bands in relaxed twisted bilayer WSe_2. Flat bands, well separated in energy, emerge at the band edges for twist angles θ near 0° and 60°. For θ near 0°, the interlayer hybridization together with a moiré potential determines the electronic structure. The bands near the valence band edge have nontrivial topology, with Chern numbers equal to $+1$ or -1. We propose that the nontrivial topology of the first band can be probed experimentally for twist angles less than a critical angle of 3.5°. For θ near 60°, the flattening of the bands arising from the K point of the unit cell Brillouin zone is a result of atomic rearrangements in the individual layers. Our findings on the flat bands and the localization of their wave functions for both ranges of θ match well with recent experimental observations.

DOI: 10.1103/PhysRevB.105.L081108

I. INTRODUCTION

Twisted bilayer transition metal dichalcogenides (TMDs) have recently gained attention as potential platforms for hosting correlated phases and novel excitonic properties [1–20]. The absence of a "magic angle" in twisted TMDs [21–25] makes the experimental realization of flat bands [1,2] easier compared with twisted bilayer graphene. Large spin-orbit coupling can strongly influence the electronic structure of the moiré superlattice (MSL) and cause the bands to have nontrivial topological character. Within the TMD family, WSe_2 is a prototypical example with large spin-orbit coupling, making twisted WSe_2 bilayers ($tWSe_2$) especially interesting.

Recent spectroscopic imaging and transport measurements in $tWSe_2$ show evidence of flat bands [1,2,26]. As we discuss in detail in this Research Letter, the flat bands at the valence band (VB) edge in the MSL of $tWSe_2$ arise from the bands near the K points of the unit cell Brillouin zone (UBZ), *unlike* in other TMDs such as MoS_2. The origin and electronic structure of the flat bands arising from the K point are different from those due to the Γ point; the latter are primarily determined by the interlayer hybridization, whereas the former are a result of the "moiré potential," the additional effective potential generated due to the relaxation of the atoms upon twisting. The spin character of the flat bands is determined by the spin-valley locking in WSe_2. Due to the large spin-orbit splitting and the spin-valley locking at the K or K' valley, $tWSe_2$ is a good platform for exploring opportunities for spintronics as well as valleytronics.

Most theoretical studies on $tWSe_2$ to date [27–32] have been based on continuum models [33,34]. In this Research Letter, we study flat bands in the *relaxed* MSL of $tWSe_2$ using density functional theory (DFT). We focus our study on twist angles θ near 0°, ranging from 7.3° to 1.89°, and near 60°, ranging from 52.7° to 58.11°. We find several well-separated flat bands near the band edges in $tWSe_2$ for both ranges of θ. The spin-orbit splitting of the monolayer bands is preserved in $tWSe_2$. *Both* the moiré potential and the interlayer hybridization govern the electronic structure of $tWSe_2$ with θ near 0°; in contrast, the flat bands in $tWSe_2$ with θ near 60° primarily result from the moiré potential alone. Flat bands near the VB edge for θ near 0° are topologically nontrivial [33]. This stems from the nonzero Berry curvature at the K valleys of the UBZ. We fit the bands to the continuum model [33]; the obtained parameters thus include the effect of structural relaxation of the MSL. We also find flat bands arising from the Γ point of the UBZ *inside the VB continuum* for both ranges of θ. The spatial localization of these flat bands is in excellent agreement with recent scanning tunneling microscopy (STM) measurements [1].

We note that larger deviations of θ from 0° or 60° lead to smaller moiré supercells. In such systems, the effect of kinetic energy is more prominent compared with the moiré effect, and the bands in the moiré Brillouin zone (MBZ) are primarily a result of the band folding. Conversely, the closer θ is to 0° or 60°, the larger the moiré supercell, and the flatter the bands, increasing the possibilities for interesting strong correlation phenomena, with scope for additional richness in the presence of bands with nontrivial topology. Hence we focus in this Research Letter on $tWSe_2$ with θ near 0° and 60°. It is to be noted that 30° $tWSe_2$ can give rise to quasicrystalline order [35,36], and we hope to study such systems in the future.

Our electronic structure calculations were performed using the atomic-orbital basis as implemented in the SIESTA package [37]. The commensurate $tWSe_2$ structures are generated using the TWISTER code [21] and relaxed using classical force fields as implemented in Large-Scale Atomic/Molecular Massively Parallel Simulator (LAMMPS) [38–41] (for other details, see Supplemental Material (SM) [42]). The relaxation patterns agree well with previous studies on other TMDs [22,43–45].

*Present address: Department of Physics, University of California at Berkeley, California 94720, USA, and Materials Sciences Division, Lawrence Berkeley National Laboratory, Berkeley, California 94720, USA.

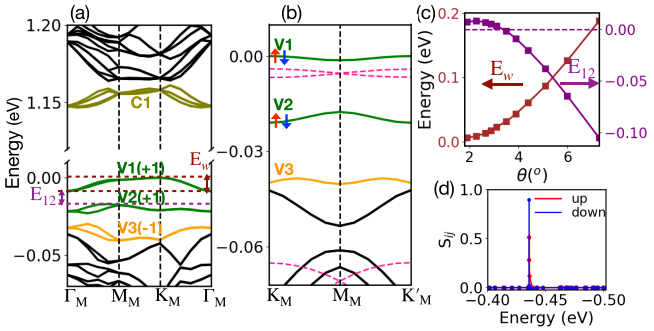

FIG. 1. (a) Band structure of 2.28° $tWSe_2$ along the path Γ_M-M_M-K_M-Γ_M with the VB maximum set to zero. (b) Bands near the VB edge along the path K_M-M_M-K'_M. The spin orientations of the first two bands, each doubly degenerate, are indicated by red and blue arrows. The pink dashed lines represent the band structure of the relaxed-MSL monolayer. For ease of viewing, the VB maximum of the monolayer has been set to −4 meV. (c) Variation of E_W (brown line) and E_{12} (purple line) with θ. (d) Variation of S_{ij} with energy. The red and blue lines represent spin-up and spin-down states, respectively.

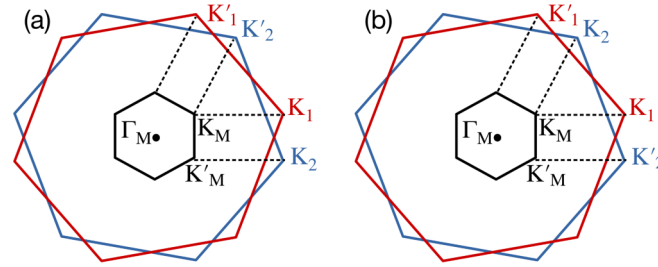

FIG. 2. (a) Schematic of the folding relation of the UBZ to the MBZ for $tWSe_2$ with θ near 0°. The small black hexagon represents the MBZ, and the red and blue hexagons represent the UBZ for the two layers, respectively. The K and K' points in all the Brillouin zones are shown. The subscripts 1 and 2 stand for the two layers. (b) Same as above for $tWSe_2$ with θ near 60°.

MSLs with θ near 0° consist of regions with three high-symmetry stackings: AA, AB, and BA (also known as 3R, $B^{W/Se}$, and $B^{Se/W}$, respectively), as well as bridge (Br) regions (the transition regions from one such stacking to another; see SM [42]). MSLs with θ near 60° consist of three other high-symmetry stackings: AA′, A′B, and AB′ (also known as 2H, $B^{Se/Se}$, and $B^{W/W}$, respectively), as well as the bridge (Br) regions. We have performed separate calculations of WSe_2 bilayers with the above high-symmetry stackings, using DFT [46–50] as well as *GW* techniques [42,51–54], and find the VB maximum to be at the K point of the UBZ. It is to be noted here that the relative positions of the VB edge at Γ and K and hence the position of the VB maximum in bilayer WSe_2 depend strongly on the interlayer separation [42,55–57]. Recently, there has been a study which suggests that the flat bands in $tWSe_2$ at the VB edge are due to the Γ point of the UBZ [58]. Nevertheless, experimental findings on $tWSe_2$ show that the bands at the VB edge arise from the K point of the UBZ, and we find the same.

II. ELECTRONIC STRUCTURE OF $tWSe_2$ WITH θ NEAR 0°

Figure 1 presents our results for the band structures of $tWSe_2$ for θ near 0°. For such θ values, bands near the K_M point of the moiré MBZ (subscript M denotes **k** points in the MBZ) arise from the monolayer bands near the K and K' points of the UBZ of the two layers. The zone folding relation is illustrated in Fig. 2(a). As the monolayer VB maxima at the K and K' points have antiparallel spins, the VB maximum at the K_M point is doubly degenerate, with antiparallel spins. Figure 1(a) shows the bands for the 2.28° $tWSe_2$. Twofold degenerate bands with opposite spins are evident near the VB edge (V1, V2, and V3). These first few VBs are shown along the path K_M-M_M-K'_M in Fig. 1(b). There is always a gap between V1 and V2, even at the M_M point, due to the interlayer hybridization [Fig. 1(b)]; this is clear from the fact that the bands for the relaxed-MSL monolayer (i.e., without interlayer interaction but with the structural relaxation effects of the MSL included) along the same path [pink dashed lines in Fig. 1(b)] show a band crossing at M_M.

To study the topological aspects of the band structure, we have calculated the Chern number C_n for the first few bands near the VB edge. As the bands are doubly degenerate with antiparallel spin, we differentiate between the flat bands by following the spin. For this purpose we calculate the expectation value of the Pauli matrices for the first few bands at the VB edge and find that $\langle\sigma_z\rangle$ is approximately ±1 and $\langle\sigma_x\rangle$ and $\langle\sigma_y\rangle$ are nearly zero. We consider the band with $\langle\sigma_z\rangle = +1$ (−1) as the spin-up (spin-down) band. We generate the Bloch wave functions using DFT on a regular k grid in the MBZ and compute the C_n's [42,59,60]. The larger θ is, the denser is the k grid we have used. For $\theta = 1.89°$, we compute the C_n using a 6×6 k grid in the MBZ and the C_n are +1, +1, and +1, respectively, for the V1, V2, and V3 spin-up bands. For $2.28° \geqslant \theta > 4.4°$, C_n are +1, +1, −1 for V1, V2, and V3, respectively. For $\theta \geqslant 4.4°$ we report C_n for the first two isolated bands (+1 for both V1 and V2) only. The spin-down bands have C_n's with opposite signs. It is important to note that the first band is topologically trivial when calculated for unrelaxed $tWSe_2$, and the second band overlaps with other bands. The θ variation of the bandwidth of V1 (E_W) and the minimum energy gap between V1 and V2 (E_{12}) are shown in Fig. 1(c). While E_W increases monotonically with θ, E_{12} becomes negative at 3.5°. While nonzero C_n is found for a large range of θ, the negative E_{12} limits the range of angles for observing quantum spin-Hall insulating states of the first band in $tWSe_2$ [61,62]. Furthermore, the quantum spin-Hall state can be probed for the first two bands till 4.4°. We have compared our DFT results with the continuum model [33]. While the latter gives the Chern number of the first two bands consistent with DFT for all θ, it is unable to describe the DFT-calculated C_n of the third band [42].

Figure 1(a) also shows six split-off bands (C1) near the conduction band (CB) edge. These bands are degenerate at Γ_M with three having spin up and other three having spin down. The Q valley of the UBZ gives rise to these bands near the CB minima in the MBZ. The bands near the CB minima at alternate Q points of the UBZ have antiparallel spins. This determines the spin character of C1 as well as of the next set

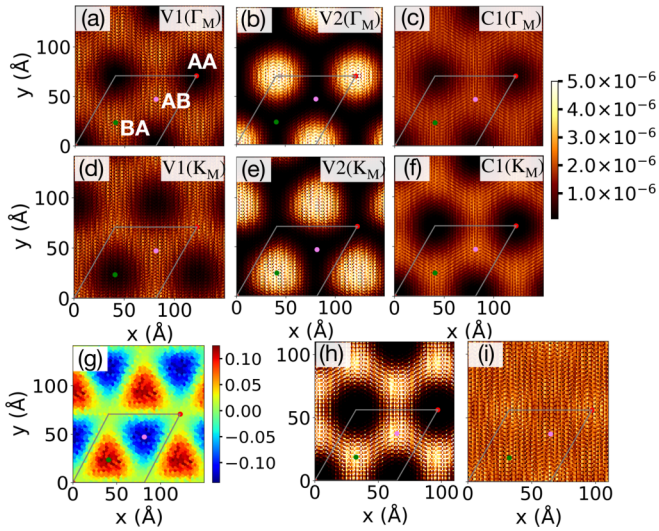

FIG. 3. (a), (b), and (c) [(d), (e), and (f)] Distribution of $|\psi_{\Gamma_M}(\mathbf{r})|^2$ [$|\psi_{K_M}(\mathbf{r})|^2$] averaged along the out-of-plane (z) direction for the V1, V2, and C1 bands for $\theta = 2.28^\circ$ $tWSe_2$. (g) Moiré potential (in eV) of the relaxed-MSL monolayer. (h) LDOS (normalized) of the first flat band arising from the Γ point of the UBZ. (i) LDOS of the V1 states arising from the K point of the UBZ. The high-symmetry stacking regions are as marked in (a).

of bands near the CB minimum in the MBZ, which are also sixfold degenerate at Γ_M.

In order to clarify the nature of the spin-orbit splitting in the MSL, we have calculated the matrix elements of the spin-raising or spin-lowering operator $S^{\pm}(= S_x \pm iS_y)$: $S_{ij} = \langle \psi_i^{K_M} | S^{\pm} | \psi_j^{K_M} \rangle$ where $\psi_i^{K_M}$ and $\psi_j^{K_M}$ are two wave functions at the K_M point of the MBZ. We calculate the S_{ij} for i corresponding to the two highest energy states of the VB edge (at the K_M point) and for j corresponding to the states within the energy range 0–500 meV below. We find states 436 meV below the VB maximum for which S_{ij} is large [Fig. 1(d)]. This implies that the atomic spin-orbit splitting remains essentially unchanged in MSLs.

Wave-function localization. Next, we discuss the localization of the wave functions of the bands mentioned above, using false-color plots of the probability $|\psi_{\mathbf{k}}(\mathbf{r})|^2$ inside the MSL, for special choices of $\mathbf{k}$. (The localization characteristics vary with the choice of $\mathbf{k}$.) Figures 3(a) and 3(b) depict the localization of the wave functions corresponding to V1 and V2, respectively, at the Γ_M point; the V1 wave function shows a hexagonal pattern avoiding AA stacking regions and occupying the AB and BA regions, while the V2 wave function is localized in the AA regions. Figures 3(d) and 3(e) show the localization of V1 and V2 at K_M for *one spin orientation* (say, spin down); V1 localizes on AA and AB regions, while V2 does so on BA regions. At K_M, the localization of the other spin (spin up, not shown) is complementary; V1 localizes on AA and BA regions, and V2 localizes on AB regions. Figures 3(c) and 3(f) depict the localization of the C1 wave functions at Γ_M and K_M, respectively. In both cases, C1 localizes on AB and BA regions as the CB minimum at the Q valley in the UBZ has the lowest energy for AB and BA stackings.

A complimentary picture of the localization is provided by the coarse-grained "moiré potential" V_M [22] of a relaxed-MSL monolayer. The coarse-grained potential is obtained by averaging the potential in a Voronoi cell centered at the W atoms (x_W, y_W) in each layer:

$$V_M(x_W, y_W) = \frac{\int_{\Omega_{\rm Vor}(x_W, y_W)} V(x, y, z) d\mathbf{r}}{\Omega_{\rm Vor}(x_W, y_W)} - \bar{V}. \quad (1)$$

Here, $V(x, y, z)$ is the local potential obtained from the DFT calculation, and $\bar{V}$ is its mean. Figure 3(g) depicts the moiré potential of one of the layers. The variation of the potential is driven by the strain and relaxation patterns. The resulting V_M shows an alternate arrangement of maxima and minima in a hexagonal shape centered on the AA regions. The other layer has a similar pattern with the positions of maxima and minima interchanged. The moiré potential along with the interlayer hybridization determines the electronic structure of the relaxed MSL of $tWSe_2$ for θ near 0°.

Comparison with experiment. STM images of 3° $tWSe_2$ [1] showed signatures of flat bands derived from the Γ point of the UBZ and the local density of states (LDOS) corresponding to these bands. We find flat bands arising from the Γ point of the UBZ *inside the VB continuum* [42]. The LDOS associated with these Γ-derived states localizes strongly on AB, BA, and Br regions, forming a hexagonal pattern [Fig. 3(h)]. This is in excellent agreement with the STM image of the Γ-derived flat band [1]. In contrast, the LDOS of V1, which arises due to the K point of the UBZ, and is shown in Fig. 3(i), is delocalized in the moiré unit cell, also consistent with experimental findings [1].

III. ELECTRONIC STRUCTURE OF $tWSe_2$ WITH θ NEAR 60°

We next discuss our findings for the electronic structure and the wave functions of the relaxed MSLs obtained for θ near 60°.

Figure 4(a) depicts the band structure for the 57.72° MSL, with the bands near the VB and CB edges being shown more clearly in Figs. 4(b) and 4(c). Several well-separated flat bands emerge at the VB edge [Fig. 4(b)]. These bands are fourfold degenerate at the Γ_M point of the MBZ and split into two sets of twofold degenerate bands at the K_M point, with the spins of each set being parallel to each other [inset of Fig. 4(a)] but antiparallel to the spins of the other set. This is because the first set of bands at the K_M point of the MBZ arise from the VB maxima at the K points of the UBZ of the two layers, which have the same spin. The second set of bands with the opposite spin at the K_M point arises from the VBs at the K' (modulo a reciprocal lattice vector of the MSL) point of the UBZ of the two layers. This folding relation is shown in Fig. 2(b). The bands at the VB edge for θ near 60° are topologically trivial. The flat bands at the CB edge are nearly 12-fold degenerate [Fig. 4(c)] (two sets of sixfold degenerate bands with ∼4 meV separation) and originate from the doubly degenerate bands with antiparallel spins at the Q valley of the UBZ.

To further clarify the spin character of the bands, the V1 and V2 bands near the VB edge are shown along the path K_M-M_M-K'_M in the MBZ in the inset of Fig. 4(a). As can be seen, the two sets comprising the V1 bands cross each other

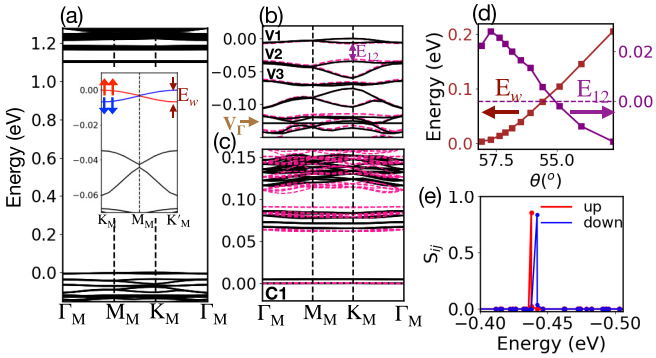

FIG. 4. (a) Band structure of 57.72° $tWSe_2$. The VB maximum is set to zero. Inset: Bands near the VB edge along the K_M-M_M-K'_M path. The spin characteristic of the first two bands is shown in red and blue. (b) and (c) Bands near the VB and CB edges in (a) for the relaxed-MSL bilayer (black lines) and the relaxed-MSL monolayer (pink dashed lines). The VB maxima and CB minima are set to zero as appropriate. (d) E_W and E_{12} vs the twist angle θ. (e) S_{ij} vs energy for spin-up (red) and spin-down (blue) states.

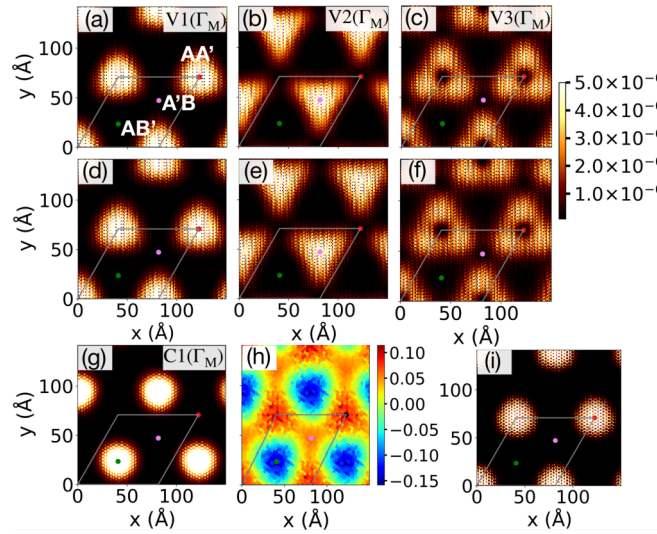

FIG. 5. (a), (b), and (c) [(d), (e), and (f)] Depiction of $|\psi_{\Gamma_M}(\mathbf{r})|^2$ averaged along the out-of-plane (z) direction for V1, V2, and V3 (see Fig. 4) bands from the relaxed-MSL bilayer (relaxed-MSL monolayer) for $\theta = 57.72°$ $tWSe_2$. (g) Depiction of $|\psi_{\Gamma_M}(\mathbf{r})|^2$ averaged along the z direction for the C1 band of the relaxed-MSL bilayer for $\theta = 57.72°$ $tWSe_2$. (h) Moiré potential (in eV) for the relaxed-MSL monolayer. (i) LDOS for bands arising from the Γ point of the UBZ.

at the M_M point of the MBZ and have opposite ordering at the K'_M point. Figure 4(d) shows the variation with θ of the energy gap E_W at the K_M point between these two sets of bands (brown line) and of the minimum energy gap between V1 and V2 (E_{12}) (purple line). As can be seen from the figure, E_{12} becomes negative for $\theta \gtrsim 54.9°$, and E_W, which also denotes the bandwidth of V1 as both the maximum value and minimum value of V1 are at K_M, decreases with increasing MSL size. It is worth emphasizing that E_W is not a spin-orbit splitting but arises due to band folding. This becomes evident if we look for the atomic spin-orbit partner of the V1 state at the K_M point by calculating the matrix elements S_{ij} as discussed before. We find large S_{ij} for states ∼440 meV below the corresponding states at the VB edge [Fig. 4(e)].

Wave-function localization. The localization of the wave functions at the Γ_M point of the MBZ for the flat bands labeled V1, V2, and V3 in Fig. 4(b) is depicted in Figs. 5(a)–5(c), and that for the CB minimum [C1 in Fig. 4(c)] is depicted in Fig. 5(g). We find that V1 localizes on the AA′ stacking regions, whereas V2 and V3 localize on the A′B and AA′ stacking regions, respectively. This is qualitatively different from what happens in other twisted homobilayer TMDs [21]. C1 has a very small dispersion (<1 meV) and localizes strongly on the AB′ stacking regions.

Comparison with relaxed monolayer. Some insight into the various features of the above band structure can be obtained by noting that the local stacking at *any* given point of the $tWSe_2$ MSL with θ near 60° preserves the inversion symmetry as seen in the high-symmetry stackings: AA′, AB′, and A′B (see SM [42]). This inversion symmetry, together with time-reversal symmetry, makes the effective interlayer interaction zero at the K point of the UBZ [33]. It is also responsible for the trivial topology of these bands. In view of this, and the fact that the flat bands near the VB edge arise from the K point of the UBZ, we have studied the electronic structure of the relaxed-MSL monolayer. The results are shown as pink dashed lines in Fig. 4(b) (VB edge) and Fig. 4(c) (CB edge). Clearly, the flat bands near the VB edge originating from the bilayer MSL are remarkably similar to those from the relaxed-MSL monolayer, with close agreement with respect to the dispersion of the bands, as well as the separation between them. This implies that the flat bands near the VB edge originate primarily from the in-plane strains and not from the interlayer hybridization. The first three wave functions at the VB edge of the relaxed-MSL monolayer are depicted in Figs. 5(d)–5(f), and they look the same as those of the MSL bilayer. On the other hand, the flat bands at the CB edge are derived from the Q valley of the UBZ. Although the interlayer hybridization is nonzero at the Q valley, the bands near the CB edge of bilayer MSL and of the relaxed-MSL monolayer also agree very well. Furthermore, the CB edge wave function at the Γ_M point of the relaxed monolayer localizes at the same stacking regions as that of the full MSL.

In order to further understand the wave-function localization, we have computed the moiré potential V_M of the relaxed-MSL monolayer [Fig. 5(h)]. V_M has maxima at the AA′ and A′B regions and minima at the AB′ regions, which is consistent with the holes localizing at AA′ and A′B and the electrons localizing at AB′. Hence, in the case of $tWSe_2$ with θ close to 60°, a relaxed-MSL monolayer is sufficient to account for the electronic properties of the MSL if one is interested in the first few bands at the band edges.

Flat bands arising from the Γ point of the UBZ. The monolayer band states near the Γ point of the UBZ also give rise to flat bands in the MBZ. The flat band at 129 meV *below the VB maximum* [marked as V_Γ in Fig. 4(b)] is the topmost such band. This band has a bandwidth <1 meV, and its wave function localizes strongly on the AA′ regions, similar to the findings in twisted MoS_2 [21,22]. The localization is consistent with the ordering of the VBs at the Γ point in the UBZ of the different high-symmetry stacking bilayers [42]. This

V_Γ band is twofold degenerate and has charge density in the interlayer region, unlike the states arising from the *K* point of the UBZ. The LDOS corresponding to the state at the Γ_M point of this band is shown in Fig. 5(i). STM studies on 57.5° $tWSe_2$ find Γ-derived bands localized on AA′ stacking [1] regions. Our findings on the nature and localization of the Γ-derived flat band are thus in excellent agreement with the STM results.

IV. CONCLUDING COMMENTS

In this Research Letter we have presented an extensive study of the formation of flat bands in $tWSe_2$ for θ near 0° as well as 60°, including the localization characteristics of the wave functions of these bands, using DFT. Our study includes the strong spin-orbit coupling present in this system, as well as the atomic rearrangements arising from the relaxation of the rigidly rotated bilayer system. We find topologically nontrivial bands for $tWSe_2$ near 0°, where interlayer hybridization together with the moiré potential determines the electronic structure. For θ near 60°, the moiré potential of the relaxed-MSL monolayer alone can account for the electronic structure and the localization characteristics of the first few flat bands at the band edges. Furthermore, we have identified another set of flat bands arising from the Γ point of the UBZ. Our findings are in excellent agreement with recent STM experiments. We believe that our study provides generic insights into the nature of flat bands in twisted TMD bilayers with strong spin-orbit interactions. The *K*-derived flat bands at the VB edge should prove especially valuable for investigating the spin-valley physics in twisted homobilayer TMD systems.

ACKNOWLEDGMENTS

We thank the Supercomputer Education and Research Centre (SERC) at IISc for providing the computational resources. S.K. and M.J. acknowledge discussions with Johannes Lischner and Valerio Vitale. M.J. and H.R.K. gratefully acknowledge the National Supercomputing Mission of the Department of Science and Technology, India, and the Science and Engineering Research Board of the Department of Science and Technology, India, for financial support under Grants No. DST/NSM/R&D_HPC_Applications/2021/23 and No. SB/DF/005/2017, respectively.

[1] Z. Zhang, Y. Wang, K. Watanabe, T. Taniguchi, K. Ueno, E. Tutuc, and B. J. LeRoy, Nat. Phys. **16**, 1093 (2020).
[2] L. Wang, E.-M. Shih, A. Ghiotto, L. Xian, D. A. Rhodes, C. Tan, M. Claassen, D. M. Kennes, Y. Bai, B. Kim, K. Watanabe, T. Taniguchi, X. Zhu, J. Hone, A. Rubio, A. N. Pasupathy, and C. R. Dean, Nat. Mater. **19**, 861 (2020).
[3] G. Scuri, T. I. Andersen, Y. Zhou, D. S. Wild, J. Sung, R. J. Gelly, D. Bérubé, H. Heo, L. Shao, A. Y. Joe, A. M. Mier Valdivia, T. Taniguchi, K. Watanabe, M. Lončar, P. Kim, M. D. Lukin, and H. Park, Phys. Rev. Lett. **124**, 217403 (2020).
[4] S. Brem, K.-Q. Lin, R. Gillen, J. M. Bauer, J. Maultzsch, J. M. Lupton, and E. Malic, Nanoscale **12**, 11088 (2020).
[5] T. I. Andersen, G. Scuri, A. Sushko, K. D. Greve, J. Sung, Y. Zhou, D. S. Wild, R. J. Gelly, H. Heo, K. Watanabe, T. Taniguchi, P. Kim, H. Park, and M. D. Lukin, Nat. Mater. **20**, 480 (2021).
[6] A. M. van der Zande, J. Kunstmann, A. Chernikov, D. A. Chenet, Y. You, X. Zhang, P. Y. Huang, T. C. Berkelbach, L. Wang, F. Zhang, M. S. Hybertsen, D. A. Muller, D. R. Reichman, T. F. Heinz, and J. C. Hone, Nano Lett. **14**, 3869 (2014).
[7] S. Carr, D. Massatt, S. Fang, P. Cazeaux, M. Luskin, and E. Kaxiras, Phys. Rev. B **95**, 075420 (2017).
[8] M.-L. Lin, Q.-H. Tan, J.-B. Wu, X.-S. Chen, J.-H. Wang, Y.-H. Pan, X. Zhang, X. Cong, J. Zhang, W. Ji, P.-A. Hu, K.-H. Liu, and P.-H. Tan, ACS Nano **12**, 8770 (2018).
[9] J. Kang, J. Li, S.-S. Li, J.-B. Xia, and L.-W. Wang, Nano Lett. **13**, 5485 (2013).
[10] I. Maity, M. H. Naik, P. K. Maiti, H. R. Krishnamurthy, and M. Jain, Phys. Rev. Research **2**, 013335 (2020).
[11] R. Debnath, I. Maity, R. Biswas, V. Raghunathan, M. Jain, and A. Ghosh, Nanoscale **12**, 17272 (2020).
[12] D. Soriano and J. L. Lado, J. Phys. D: Appl. Phys. **53**, 474001 (2020).
[13] M. Förg, A. S. Baimuratov, S. Y. Kruchinin, I. A. Vovk, J. Scherzer, J. Förste, V. Funk, K. Watanabe, T. Taniguchi, and A. Högele, Nat. Commun. **12**, 1656 (2021).
[14] Z. Li, X. Lu, D. F. C. Leon, J. Hou, Y. Lu, A. Kaczmarek, Z. Lyu, T. Taniguchi, K. Watanabe, L. Zhao, and L. Yang, ACS Nano **15**, 1539 (2021).
[15] J. Wang, Q. Shi, E.-M. Shih, L. Zhou, W. Wu, Y. Bai, D. A. Rhodes, K. Barmak, J. C. Hone, C. R. Dean, and X.-Y. Zhu, Phys. Rev. Lett. **126**, 106804 (2021).
[16] X. Lu, X. Li, and L. Yang, Phys. Rev. B **100**, 155416 (2019).
[17] A. Y. Joe, L. A. Jáuregui, K. Pistunova, Z. Lu, D. S. Wild, G. Scuri, K. D. Greve, R. J. Gelly, Y. Zhou, J. Sung, A. M. M. Valdivia, A. Sushko, T. Taniguchi, K. Watanabe, D. Smirnov, M. D. Lukin, H. Park, and P. Kim, Phys. Rev. B **103**, L161411 (2021).
[18] L. Zhang, Z. Zhang, F. Wu, D. Wang, R. Gogna, S. Hou, K. Watanabe, T. Taniguchi, K. Kulkarni, T. T. S. Kuo, S. R. Forrest, and H. Deng, Nat. Commun. **11**, 5888 (2020).
[19] H. Li, S. Li, M. H. Naik, J. Xie, X. Li, J. Wang, E. Regan, D. Wang, W. Zhao, S. Zhao, S. Kahn, K. Yumigeta, M. Blei, T. Taniguchi, K. Watanabe, S. Tongay, A. Zettl, S. G. Louie, F. Wang, and M. F. Crommie, Nat. Mater. **20**, 945 (2021).
[20] Y. Luo, R. Engelke, M. Mattheakis, M. Tamagnone, S. Carr, K. Watanabe, T. Taniguchi, E. Kaxiras, P. Kim, and W. L. Wilson, Nat. Commun. **11**, 4209 (2020).
[21] M. H. Naik and M. Jain, Phys. Rev. Lett. **121**, 266401 (2018).
[22] M. H. Naik, S. Kundu, I. Maity, and M. Jain, Phys. Rev. B **102**, 075413 (2020).
[23] M. Angeli and A. H. MacDonald, Proc. Natl. Acad. Sci. USA **118**, e2021826118 (2021).
[24] L. Xian, M. Claassen, D. Kiese, M. M. Scherer, S. Trebst, D. M. Kennes, and A. Rubio, Nat. Commun. **12**, 5644 (2021).
[25] Y. Zhang, T. Liu, and L. Fu, Phys. Rev. B **103**, 155142 (2021).

[26] M. Huang, Z. Wu, J. Hu, X. Cai, E. Li, L. An, X. Feng, Z. qing Ye, N. Lin, K. T. Law, and N. Wang, arXiv:2006.05615 [cond-mat.mes-hall].
[27] Z. Bi and L. Fu, Nat. Commun. **12**, 642 (2021).
[28] J.-X, Hu, C.-P. Zhang, Y.-M. Xie, and K. T. Law, arXiv:2004.14140 [cond-mat.mes-hall].
[29] H. Pan, F. Wu, and S. Das Sarma, Phys. Rev. Research **2**, 033087 (2020).
[30] H. Pan, F. Wu, and S. Das Sarma, Phys. Rev. B **102**, 201104(R) (2020).
[31] H. Pan and S. Das Sarma, Phys. Rev. Lett. **127**, 096802 (2021).
[32] T. Devakul, V. Crépel, Y. Zhang, and L. Fu, Nat. Commun. **12**, 6730 (2021).
[33] F. Wu, T. Lovorn, E. Tutuc, I. Martin, and A. H. MacDonald, Phys. Rev. Lett. **122**, 086402 (2019).
[34] H. Tang, S. Carr, and E. Kaxiras, Phys. Rev. B **104**, 155415 (2021).
[35] P. Stampfli, Helv. Phys. Acta **59**, 126040783 (1986).
[36] S. J. Ahn, P. Moon, T.-H. Kim, H.-W. Kim, H.-C. Shin, E. H. Kim, H. W. Cha, S.-J. Kahng, P. Kim, M. Koshino, Y.-W. Son, C.-W. Yang, and J. R. Ahn, Science **361**, 782 (2018).
[37] J. M. Soler, E. Artacho, J. D. Gale, A. García, J. Junquera, P. Ordejón, and D. Sánchez-Portal, J. Phys.: Condens. Matter **14**, 2745 (2002).
[38] S. Plimpton, J. Comput. Phys. **117**, 1 (1995).
[39] F. H. Stillinger and T. A. Weber, Phys. Rev. B **31**, 5262 (1985).
[40] A. N. Kolmogorov and V. H. Crespi, Phys. Rev. B **71**, 235415 (2005).
[41] M. H. Naik, I. Maity, P. K. Maiti, and M. Jain, J. Phys. Chem. C **123**, 9770 (2019).
[42] See Supplemental Material at http://link.aps.org/supplemental/10.1103/PhysRevB.105.L081108 for computational details, high symmetry stackings, structural aspects of MSL, calculation of Chern number, comparison with experiments and moiré continuum Hamiltonian.
[43] V. V. Enaldiev, V. Zólyomi, C. Yelgel, S. J. Magorrian, and V. I. Fal'ko, Phys. Rev. Lett. **124**, 206101 (2020).
[44] I. Maity, P. K. Maiti, H. R. Krishnamurthy, and M. Jain, Phys. Rev. B **103**, L121102 (2021).
[45] S. Carr, S. Fang, Z. Zhu, and E. Kaxiras, Phys. Rev. Research **1**, 013001 (2019).
[46] P. Giannozzi, S. Baroni, N. Bonini, M. Calandra, R. Car, C. Cavazzoni, D. Ceresoli, G. L. Chiarotti, M. Cococcioni, I. Dabo, A. D. Corso, S. de Gironcoli, S. Fabris, G. Fratesi, R. Gebauer, U. Gerstmann, C. Gougoussis, A. Kokalj, M. Lazzeri, L. Martin-Samos *et al.*, J. Phys.: Condens. Matter **21**, 395502 (2009).
[47] J. P. Perdew and A. Zunger, Phys. Rev. B **23**, 5048 (1981).
[48] H. J. Monkhorst and J. D. Pack, Phys. Rev. B **13**, 5188 (1976).
[49] V. R. Cooper, Phys. Rev. B **81**, 161104(R) (2010).
[50] J. P. Perdew, K. Burke, and M. Ernzerhof, Phys. Rev. Lett. **77**, 3865 (1996).
[51] J. Deslippe, G. Samsonidze, D. A. Strubbe, M. Jain, M. L. Cohen, and S. G. Louie, Comput. Phys. Commun. **183**, 1269 (2012).
[52] M. S. Hybertsen and S. G. Louie, Phys. Rev. B **34**, 5390 (1986).
[53] S. Ismail-Beigi, Phys. Rev. B **73**, 233103 (2006).
[54] J. Deslippe, G. Samsonidze, M. Jain, M. L. Cohen, and S. G. Louie, Phys. Rev. B **87**, 165124 (2013).
[55] Z. Gong, G.-B. Liu, H. Yu, D. Xiao, X. Cui, X. Xu, and W. Yao, Nat. Commun. **4**, 2053 (2013).
[56] G.-B. Liu, D. Xiao, Y. Yao, X. Xu, and W. Yao, Chem. Soc. Rev. **44**, 2643 (2015).
[57] M. H. Naik and M. Jain, Phys. Rev. B **95**, 165125 (2017).
[58] V. Vitale, K. Atalar, A. A. Mostofi, and J. Lischner, 2D Mater. **8**, 045010 (2021).
[59] T. Fukui, Y. Hatsugai, and H. Suzuki, J. Phys. Soc. Jpn. **74**, 1674 (2005).
[60] R. Zhao, G.-D. Xie, M. L. N. Chen, Z. Lan, Z. Huang, and W. E. I. Sha, Opt. Express **28**, 4638 (2020).
[61] C. L. Kane and E. J. Mele, Phys. Rev. Lett. **95**, 226801 (2005).
[62] C. L. Kane and E. J. Mele, Phys. Rev. Lett. **95**, 146802 (2005).